CCS Chemistry

RESEARCH ARTICLE

Received: Mar. 25, 2024 | Accepted: June 12, 2024 | Published: July 27, 2024

The Synergetic Effect of Dual Active Sites in ZnO-ZrO_2 Catalyst for CO_2 Hydrogenation to Methanol

Jijie Wang[1†], Shunning Li[2†], Wei Liu[1†], Yinguo Xiao[2], Zhendong Feng[1,3], Xianhui Liang[2], Shan Tang[1,3], Guanna Li[4], Cheng Dong[2], Feng Pan[2*] & Can Li[1,3*]

[1]*State Key Laboratory of Catalysis, Dalian Institute of Chemical Physics, Chinese Academy of Sciences, Dalian 116023*, [2]*School of Advanced Materials, Peking University Shenzhen Graduate School, Shenzhen 518055*, [3]*University of Chinese Academy of Sciences, Beijing 100049*, [4]*Biobased Chemistry and Technology, Wageningen University & Research, Wageningen 6700 HB*

**Corresponding authors: panfeng@pkusz.edu.cn; canli@dicp.ac.cn ;* [†]J. Wang, S. Li, and W. Liu contributed equally to this work.

Cite this: *CCS Chem.* **2024**, 6, 2996–3007
DOI: 10.31635/ccschem.024.202404243

The reaction of CO_2 hydrogenation to methanol is a typical reaction requiring simultaneous activation of CO_2 and H_2. The ZnO-ZrO_2 solid solution catalyst has been demonstrated to be an excellent catalyst, and the dual active site of Zn-O-Zr has been a key active site. However, the actual surface configuration of Zn and Zr and how CO_2 and H_2 are activated on the active sites remain unclear. Here, our research shows that there is a synergetic effect of dual active sites in the ZnO-ZrO_2 catalyst for CO_2 hydrogenation to methanol. In the 5%ZnO-ZrO_2 catalyst, which has a low density of Zn-O-Zr sites, the dominant form of zinc coordination is as an isolated Zn site. The main coordination form of 20%ZnO-ZrO_2 catalyst with moderate density of the Zn-O-Zr site is the (Zn)-O-Zr-O-(Zn) site. The main coordination form of 40% ZnO-ZrO_2 catalyst with high density of the Zn-O-Zr site is (Zn)-O-(Zn) site. The catalyst with a Zn-O-Zr site of moderate density exhibits more efficient activation of H_2 and CO_2 and a lower energy barrier for the rate-determining step, which leads to superior catalytic activity. This work discovers the synergetic effect of the Zn-O-Zr sites in the ZnO-ZrO_2 catalyst for CO_2 hydrogenation to methanol and sheds light on the importance of the active site synergetic effect on multisite catalysts.

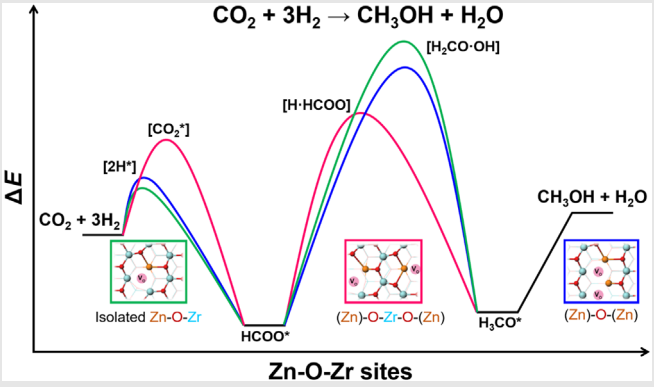

Keywords: **CO_2 hydrogenation, methanol synthesis, dual active sites, synergetic effect, ZnO-ZrO_2 catalyst**

Introduction

The hydrogenation of CO_2 with renewable H_2 produced by solar and wind power is not only one of the most effective solutions to achieve net-zero carbon commitments but is also important in both academic and industrial contexts as the means of synthesizing value-added chemicals. Among hydrogenation products, methanol (CH_3OH) is the one for achieving methanol economy[1] and is particularly desirable due to its

capability and use as an easily transportable fuel and a precursor in the production of olefins and aromatics. Therefore, the methanol produced by the hydrogenation of CO_2 with renewable H_2 is called "Liquid Sunshine Methanol."[2,3] The conversion of CO_2 and H_2 to methanol requires simultaneous activation of both reactants on sites in close proximity. This requirement motivates research efforts to pursue bifunctional active sites in heterogeneous catalysts, which can be rendered by solid solution formation.[4–7] Bifunctional active sites possess dual catalytic sites that can independently regulate two activation processes and accommodate different reaction intermediates, while at the same time they work in synergy to steer the reaction towards the targeted product. Despite the recognized importance of bifunctional active sites, elucidating the detailed bifunctional reaction mechanism remains a huge challenge due to the difficulties in characterizing the nanoscale regimes at the surfaces and building the correct atomic configurations that enable excellent catalytic performance.

Aided by advanced characterization technologies and theoretical simulation, the above challenges have been partially met on the $Cu/ZnO/Al_2O_3$ catalyst,[8–13] which is a prototypical system for studying promotional interactions in the CO_2/CO-to-methanol reaction. A conceptual picture of Zn incorporation at the surfaces of Cu nanoparticles emerged after extensive investigation of this catalyst, which revealed the synergy of bifunctional Cu-Zn sites and the essential role of Zn coverage at the Cu metal surface in boosting the methanol synthesis activity.[10–13] However, the poor stability of Cu-based catalysts is still a substantial problem confronting their practical application. Moreover, it is hard to achieve both satisfactory selectivity and high stability on nearly all the recently proposed catalysts.[14–19] By comparison, ZnO-ZrO_2 solid solution is renowned for its capability to catalyze the CO_2-to-methanol reaction in a fixed-bed reactor with exceptional selectivity and stability.[4] However, current studies still fall short in understanding the underlying active site and reaction mechanism. The standing challenge resides in identifying the key catalytic sites on oxide surfaces, which are far more complex than those on metal alloy surfaces. Although it was assumed that the Zn-Zr pair site bridged by an O ion[20,21] or the ZnO_x/ZrO_2 interface[22–25] was responsible for the catalytic performance, but that does not fully explain the observed trends of activity and selectivity as a function of Zn content. Given the recent success in industrial application of ZnO-ZrO_2 solid solution catalysts (Supporting Information Figure S1), it is urgently required that we unravel the local structure of their catalytic sites, which may further inspire the development of existing oxide catalysts and the design of new ones.

Herein, we investigated the compositional dependence of catalytic sites on the surface structure of ZnO-ZrO_2 solid solution. Through an interplay of theory and in-situ experiments, we disclose that with the increase of Zn concentration in ZnO-ZrO_2 catalyst, the density of the Zn-O-Zr site rises and shows a synergetic effect between one Zn-O-Zr site and another. We set up a descriptor which called the link distance (LD)[26,27] between neighboring Zn ions at the surface to illustrate the active site density effect on the catalytic reaction, thus deciding the overall compositional trends of activity and selectivity. In particular, an appropriate value of 4 for LD (with four consecutive chemical bonds between the neighboring Zn ions), which corresponds to a configuration of (Zn)-O-Zr-O-(Zn) and can result in a much lower activation barrier than LD = 2 (corresponding to (Zn)-O-(Zn) configuration) and LD ≥ 6 (approximated as an isolated Zn dopant). The evolution of this atomic-scale structure as a function of Zn content matches well with the observed activity/selectivity maximum at the compositions close to about 20% ZnO-ZrO_2 (Zn/(Zn+Zr) = 20%). This discovery may guide the way to further optimization of surface structures for metal oxide solid solution catalysts.

Experimental Methods

Catalyst preparation

A series of *x*%ZnO-ZrO_2 catalysts (*x*% represents the molar percentage of Zn, metal base) were prepared by the coprecipitation method. Here we take the 20%ZnO-ZrO_2 catalyst as a typical example to describe the synthesis procedures: 0.74 g Zn $(NO_3)_2 \cdot 6H_2O$ and 5.19 g Zr $(NO_3)_4 \cdot 5H_2O$ were dissolved in a flask by 100 mL deionized water. The precipitator of 100 mL aqueous solution of 2.38 g $(NH_4)_2CO_3$ was added into the aforementioned solution (at a flow rate of 3 mL/min) under vigorous stirring at 70 °C so as to form a precipitate. The suspension was continuously stirred for 2 h at 70 °C, followed by cooling down to room temperature and filtering, washing with deionized water three times. The filtered sample was dried at 110 °C for 4 h and calcined at 500 °C in static air for 3 h. Other *x*%ZnO-ZrO_2 catalysts were prepared following the same method. All catalysts were pressed, crushed, and sieved to the size of 40–80 mesh for the activity evaluation.

Catalyst evaluation

The activity tests of the catalysts for CO_2 hydrogenation to methanol were carried out in a tubular fixed-bed continuous-flow reactor equipped with gas chromatography (GC). All catalysts were pressed, crushed, and sieved to the size of 40–80 mesh for the activity evaluation. Before the reaction, the catalyst (0.1 g, diluted with 0.4 g quartz sand) was pretreated in a H_2 or N_2 stream (0.1 MPa and 20 mL/min) at given temperatures. The reaction was conducted under reaction conditions of 2.0–5.0 MPa, 200–400 °C, $V(H_2)/V(CO_2)/V(Ar)$ = 72/24/4, and gas

DOI: 10.31635/ccschem.024.202404243
Citation: *CCS Chem.* **2024**, 6, 2996–3007
Link to VoR: https://doi.org/10.31635/ccschem.024.202404243

hour space velocity (GHSV) = 6000–24,000 mL/(g h). The exit gas from the reactor was maintained at 150 °C and immediately transported to the sampling valve of the GC (Agilent GC-7890B, Santa Clara, California, USA), which was equipped with thermal conductivity (TCD) and flame ionization detectors (FID). Propark N and 5A molecular sieve-packed columns (2 m × 1/8 inch, Agilent, Santa Clara, California, USA) were connected to TCD while TG-BOND-Q capillary columns were connected to FID. The packed columns were used for the analysis of CO_2, Ar, CO, and the capillary column (30 m × 0.32 mm × 10 μm, ThermoFisher, Waltham, Massachusetts, USA) for hydrocarbons, alcohols, and other C-containing products. CO_2 conversion [denoted as X (CO_2)] and the carbon-based selectivity [denoted as S(product)] for the carbon-containing products, including methane, methanol, and dimethyl ether, were calculated with an internal normalization method. The space-time yield of methanol was denoted as STY (CH_3OH). All data were collected in 3 h after the reaction started (unless otherwise specified).

Calculation of single pass X (CO_2), S(CH_3OH), S(CO), STY(CH_3OH) is as follows:

$$X(CO_2) = \frac{f_{CO}A_{CO} + i(f_{CH_4}A_{CH_4} + f_{CH_3OH}A_{CH_3OH} + 2f_{CH_3OCH_3}A_{CH_3OCH_3})}{f_{CO_2}A_{CO_2} + f_{CO}A_{CO} + i(f_{CH_4}A_{CH_4} + f_{CH_3OH}A_{CH_3OH} + 2f_{CH_3OCH_3}A_{CH_3OCH_3})} \quad i = \frac{f_{CH_4-TCD}A_{CH_4-TCD}}{f_{CH_4-FID}A_{CH_4-FID}}$$

$$S(CH_3OH) = \frac{if_{CH_3OH}A_{CH_3OH}}{f_{CO}A_{CO} + i(f_{CH_4}A_{CH_4} + f_{CH_3OH}A_{CH_3OH} + 2f_{CH_3OCH_3}A_{CH_3OCH_3})}$$

$$S(CO) = \frac{f_{CO}A_{CO}}{f_{CO}A_{CO} + i(f_{CH_4}A_{CH_4} + f_{CH_3OH}A_{CH_3OH} + 2f_{CH_3OCH_3}A_{CH_3OCH_3})}$$

$$STY(CH_3OH) = \frac{GHSV}{22.4} \times V\%(CO_2) \times X(CO_2) \times S(CH_3OH) \times M_{CH_3OH}$$

Catalyst characterization

Powder X-ray diffraction

The powder X-ray diffraction results were collected on a Philips PW1050/81 diffractometer (Alemlo, Netherlands) operating in Bragg-Brentano focusing geometry and using CuKα radiation (λ = 1.5418 Å) from a generator operating at 40 kV and 30 mA.

High resolution transmission electron microscopy

High resolution transmission electron microscopy (HRTEM) images were obtained with a JEM-2100 microscope (Japan Electronics Corporation), 200 kV. The samples were prepared by placing a drop of nanoparticle ethanol suspension onto a lacy support film and allowing the solvent to evaporate.

Neutron diffraction

The neutron powder diffraction experiments were performed on a time-of-flight neutron diffractometer, a general purpose powder diffractometer, at the China Spallation Neutron Source. Each powder sample was loaded into a vanadium can with 9.1 mm in diameter, and the neutron powder diffraction patterns were collected at room temperature with wavelengths ranging from 0.1 to 4.9 Å. The neutron diffraction patterns were analyzed with the Rietveld refinement method by using the FullProf program.

Aberration-corrected scanning transmission electron microscopy

The aberration-corrected scanning transmission electron microscopy (AC-STEM) was obtained on the JEM-ARM300F microscope (Japan Electronics Corporation) with image and probe correctors. Specifically, to ensure the most satisfactory noncoherent Z-contrast imaging, the experiment was performed under 300 kV to maximize the mean-free elastic scattering of incident electrons. High-angle annular dark-field (HAADF) imaging was conducted using a 10-pA probe scanning at a convergence angle of 22 mrad and collection angle of 54–220 mrad simultaneously, accompanied by collecting the annular bright-field signal at around 10–22 mrad to visualize oxygen atoms in the ZnO-ZrO_2 lattice. To reduce the risk of structural damage induced by high-energy electron irradiation, the dose rate was kept below 6.8×10^3 e · Å^{-2} · s^{-1} so as to achieve reliable atomic dopant information of zinc species embedded inside different ZrO_2 matrixes at varied dissolving concentrations. Elemental distribution analysis of ZnO-ZrO_2 samples was performed using a JED-2300T spectrometer (Japan Electronics Corporation; dual 165 mm^2 large area silicon drift detectors) equipped on ARM300F to obtain energy dispersive X-ray spectroscopy elemental mappings. Regarding the sample preparation, ZnO-ZrO_2 powders were dispersed in ethanol and subjected to ultrasonication for 10 min, followed by placing a solution droplet of nanoparticle ethanol suspension onto a lacy support film and allowing the solvent to evaporate naturally.

DOI: 10.31635/ccschem.024.202404243
Citation: *CCS Chem.* **2024**, 6, 2996–3007
Link to VoR: https://doi.org/10.31635/ccschem.024.202404243

Extended X-ray absorption fine structure

Extended X-ray absorption fine structure (EXAFS) fitting was performed using the VIPER program. The fitting was performed alternatively in k and R spaces. When in the R space, fitting was done in the (Im + Module) mode, which is mathematically equivalent to the k-fit. The Fourier-transformed data in the R space were analyzed by applying Zn-O and Zn-Zn contributions from ZnO and Zn foil references.

Inductively coupled plasma

An inductively coupled plasma (ICP) experiment was performed using ICPS-8100 from Shimadzu (Kyoto, Japan) with a wavelength range of 160–850 nm and resolution of 0.0045 nm.

Ex-situ X-ray photoelectron spectroscopy

X-ray photoelectron spectroscopy (XPS) was performed using a Thermo ESCALAB 250Xi with Al K radiation (Waltham, Massachusetts, USA) (15 kV, 10.8 mA, hν = 1486.6 eV) under ultrahigh vacuum (5×10^{-7} Pa), calibrated internally by the carbon deposit C(1s) (E_b = 284.6 eV). The system included a sample cell that can be simultaneously heated and exposed to CO_2 and H_2 gas feeds.

H_2-D_2 exchange experiment

H_2-D_2 exchange experiments were carried out in a flow reactor at 280 °C. The formation rate of HD was measured by mass signal intensity (ion current). A 0.1 g sample was reduced with 10 mL/min H_2 at 280 °C for 1 h. Subsequently, a mixture of 10 mL/min D_2 with H_2 passed over the catalyst sample. Reaction products HD, H_2, and D_2 were analysed with a mass spectrometer (GAM200, InProcess Instruments Company, Germany). The m/z mass values used are 2 for H_2, 4 for D_2, and 3 for HD.

Density functional theory calculation

All density functional theory (DFT) calculations were performed using the Vienna ab initio simulation package (VASP).[28] The generalized gradient approximation with Perdew–Burke–Ernzerhof exchange and correlation functional was used to account for the exchange-correlation energy.[29] The kinetic energy cutoff of the plane wave basis set was set to 400 eV. A Gaussian smearing of the population of partial occupancies with a width of 0.1 eV was used. The threshold for energy convergence for each iteration was set to 10^{-5} eV. Geometry optimization was assumed to be converged when forces on each atom were less than 0.05 eV/Å. The minimum-energy reaction pathways and the corresponding transition states were determined using the climbing-image nudged-elastic band method that were implemented in VASP.[30] Frequency analysis was performed by means of the finite difference method as implemented in VASP. Each transition state was confirmed by the presence of a single imaginary frequency corresponding to the specific reaction path.

The optimized lattice parameters for tetragonal ZrO_2 bulk are $a = b$ = 3.684 Å and c = 5.222 Å, which are in good agreement with the experimental values of $a = b$ = 3.612 Å and c = 5.212 Å.[31] Defect energy was defined as $E_d = E_{substitute+vacancy} - E_{pristine} + E_{ZrO2} - E_{ZnO}$, where $E_{substitute+vacancy}$ is the energy of a ZrO_2 supercell with a Zn_{Zr} substitutional dopant and an oxygen vacancy, $E_{pristine}$ is the energy of a pristine ZrO_2 supercell, E_{ZrO2} is the energy of ZrO_2 per formular unit, and E_{ZnO} is the energy of ZnO per formular unit. The most stable (101) surface of the ZrO_2 tetragonal phase was simulated by a $2 \times 3 \times 1$ supercell slab model, including four ZrO_2 sublayers, each containing two oxygen atomic layers and one Zr atomic layer. The ZrO_2 slab was separated by a vacuum layer with a thickness of 15 Å along the surface normal direction to avoid spurious interactions between periodic slab models. To take into account the effect of Zn^{2+} doping, one of the Zr^{4+}-O^{2-} moieties on the surface was replaced by a Zn^{2+} cation and an oxygen vacancy (Zn^{2+}-V_O). The atoms of the top two ZrO_2 sublayers were fully optimized, while the other two ZrO_2 sublayers at the bottom were fixed at their optimized bulk positions throughout the surface calculations. The on-site Coulomb correction for the Zr 4*d* states of ZrO_2 bulk as well as the surface was included by the DFT+U approach with a U_{eff} value of 4.0 eV. K-point grids of $8 \times 8 \times 6$ and $3 \times 5 \times 1$ generated by the Monkhorst-Pack scheme were used for sampling the Brillouin zones of the ZrO_2 bulk and the Zn-ZrO_2 supercell surface slab model, respectively.

Free energy for surface adsorbates was defined as $G = E_{DFT} + E_{ZPE} - TS$, where E_{DFT} is DFT ground state energy, E_{ZPE} is zero-point energy, T is temperature, and S is entropy. The vibrational frequencies of adsorbed species were calculated, from which the vibrational entropies (S_{vib}) and the zero-point energies (E_{ZPE}) in the Gibbs free energy were obtained within harmonic approximations using the finite difference method in VASP. For the pure gas phase, entropy from all degrees of freedom (translation, rotation, and vibration) was taken into consideration according to the experimental data at 593 K. The activation energy of a chemical reaction was defined as the energy difference between the initial and transition states, while the reaction energy was defined as the energy difference between the initial and final states.

Results and Discussion

Structures of ZnO-ZrO_2 catalysts and catalytic performances

We prepare a series of ZnO-ZrO_2 catalysts by the coprecipitation method with the optimized synthesis

DOI: 10.31635/ccschem.024.202404243
Citation: *CCS Chem.* **2024**, 6, 2996–3007
Link to VoR: https://doi.org/10.31635/ccschem.024.202404243

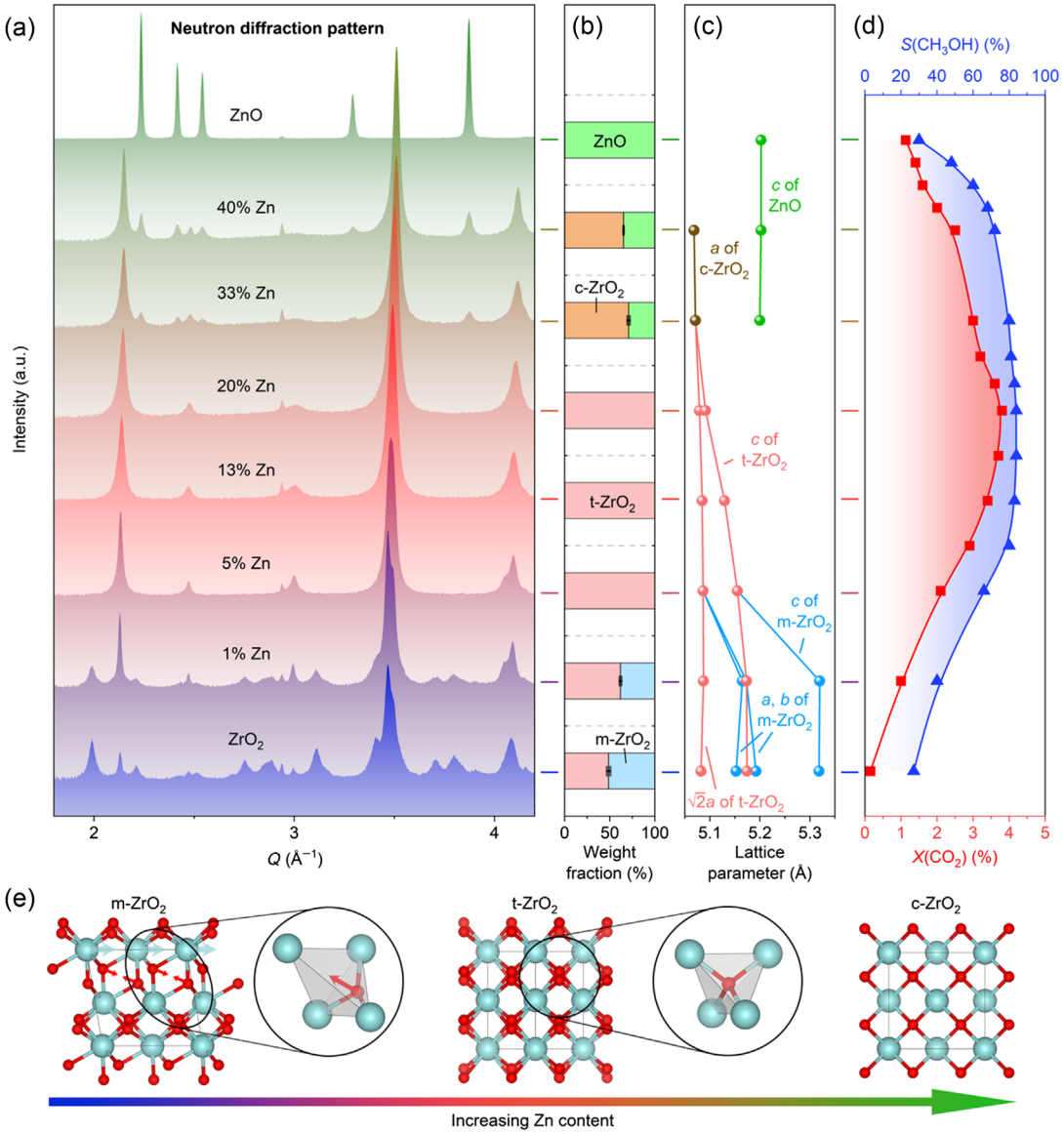

Figure 1 | *Crystal structures of ZnO-ZrO_2 solid-solution catalysts and their catalytic performances. (a) The neutron diffraction patterns as a function of Zn content. (b) The weight fraction of different phases of ZrO_2. Monoclinic, tetragonal, and cubic phases are denoted as m-ZrO_2, t-ZrO_2, and c-ZrO_2, respectively. (c) The variation of lattice parameters. (d) CO_2 conversion rate and selectivity of methanol product. Standard reaction conditions: 2.0 MPa, H_2/CO_2 = 3/1, 320 °C, GHSV = 24,000 mL/(g h), using a tubular fixed-bed reactor. (e) Evolution of crystal structure as a function of Zn content in ZnO-ZrO_2. Color code: Zr, cyan; O, red.*

conditions provided in Supporting Information. Refined neutron and X-ray diffraction patterns (Figure 1a,b and Supporting Information Figure S2 and Table S1) demonstrate that there are two phases in pure ZrO_2 at room temperature, monoclinic (majority) and tetragonal (minority). Introduction of Zn dopants ($x \geq 1\%$) induces a transition of the monoclinic phase into the tetragonal one, and all of the monoclinic phase is transformed into the tetragonal one when x reaches 5%. Further increase in Zn content ($x \geq 33\%$) leads to phase transition from tetragonal to cubic, with the simultaneous emergence of hexagonal ZnO due to phase segregation. This result is affirmed by HRTEM in Supporting Information Figure S3. We note that the transition from monoclinic to tetragonal and then to cubic is through slight displacive distortions and without long-range redistribution of atoms (Figure 1e). This feature, along with the smooth and steady evolution of lattice parameters versus Zn content at $0 \leq x \leq 40\%$ (Figure 1c), strongly supports the solid-solution structure model in this composition range, which is also confirmed by the results of refined X-ray patterns (Supporting Information Table S2). EXAFS measurements (Supporting Information Figure S4a) reveal that Zn–Zn and Zn-O-Zn shells are barely discernible at

DOI: 10.31635/ccschem.024.202404243
Citation: *CCS Chem.* **2024**, 6, 2996–3007
Link to VoR: https://doi.org/10.31635/ccschem.024.202404243

compositions before ZnO segregation, indicating that Zn atoms are dispersed as substitutional dopants to replace Zr in the ZrO_2 lattice.

The catalyst's actual elementary compositon and the surface elementary compositon were determined by ICP and XPS respectively. The results demonstrate that there is an enrichment phenomenon of Zn concentration at the catalyst surface (Supporting Information Figure S5). For $x \geq 33\%$, a steep increase of Zn content is revealed according to the XPS spectra, indicating the partial coverage of ZnO on the surface of the solid solution particles. Because the valence state of the Zn species is +2 (revealed by X-ray absorption near-edge spectroscopy in Supporting Information Figure S4b), for charge neutrality, each Zn substitutional dopant in ZrO_2 brought about the formation of a single O vacancy (V_O). Consistently, the XPS of V_O-related content (Supporting Information Figure S6) displays increasing and decreasing trends before and after x = 20%, respectively, thus substantiating the substitutional Zn_{Zr} solid solution model and the surface segregation of ZnO. By means of DFT, the formation energies of Zn_{Zr}-V_O defect complex in monoclinic, tetragonal, and cubic ZrO_2 phases were calculated to be 3.38, 1.99, and 1.57 eV, respectively. This result implies that the energy compensation of Zn_{Zr}-V_O defect formation in structures with higher symmetry is the driving force for the phase transition of ZnO-ZrO_2 solid solution.

The catalytic performance of ZnO-ZrO_2 catalysts was investigated (in a fixed-bed reactor under the conditions of H_2/CO_2=3, 24,000 h^{-1}, 2 MPa, 300 °C, details provided in Supporting Information). Methanol and CO are the main products. Figure 1d shows the CO_2 conversion rate and selectivity of methanol as a function of Zn content in the catalysts. As expected, both pure ZrO_2 and ZnO show inferior catalytic performance, while the activity is significantly enhanced when the two components are chemically mixed. The volcano patterns of both activity and selectivity raise the hypothesis that the effective catalytic sites of ZnO-ZrO_2 catalysts evolve depending on the Zn content at the surface. Especially, at bulk Zn contents between 5% and 40% where the tetragonal solid solution phase predominates, the change in Zn coordination configurations can be the governing factor for rationalizing the observed volcano patterns near the optimal composition ($x \approx 20\%$).

Coordination configurations of catalysts near the surface

X-ray energy-dispersive spectroscopy (EDS) analysis combined with AC-STEM imaging for 5%ZnO-ZrO_2, 20%ZnO-ZrO_2, and 40%ZnO-ZrO_2 samples (Figure 2a) show that at low ZnO content (5% and 20%) all the elements of zinc, oxygen, and zirconium in ZnO-ZrO_2 solid-solution catalysts are overall in homogenous distribution, in the absence of obvious atomic aggregation. At higher Zn contents, two or more Zn_{Zr} atoms (or ions) can be in a close proximity, which is fundamentally different from the case of isolated Zn_{Zr} centers. The pattern of Zn-Zr-Zn columns in a sequence, as evidenced in the HAADF image of 20% ZnO-ZrO_2 along the t-ZrO_2 <010> direction, indicates the coordination configuration of (Zn)-O-Zr-O-(Zn) (LD = 4, shown in Figure 2b) in the surface region. Along with this configuration, we also identified configurations of isolated Zn (LD ≥ 6) and (Zn)-O-(Zn) (LD = 2), the latter corresponding to a local concentrated Zn_{Zr} region that emerged due to the random distribution of Zn dopants. As compared to the 20%ZnO-ZrO_2 sample, the 5%ZnO-ZrO_2 sample shows a relatively sparse distribution of Zn dopants (Supporting Information Figure S7), with much less frequent appearance of the (Zn)-O-Zr-O-(Zn) configuration. For the 40%ZnO-ZrO_2, more (Zn)-O-(Zn) (LD = 2) configurations are observed. However, there is no evidence to exclude the configurations of LD = 4 and LD ≥ 6.

To further depict the fine structure of the ZnO-ZrO_2 surface with optimal catalytic performance, HAADF mode has been performed for the ZnO-ZrO_2 sample as shown in Figure 2c. The projected contrast reveals that there are sparse sites of weak contrast located very close to the lattice sites of Zr columns. Since in noncoherent scattering imaging, weak scattering contrast is attributed to the column composed of light atoms, these weak scattering sites are thus identified as Zn dopants at Zr sites with a small distortion that makes the Zn visible. Figure 2c directly shows the structural evidence for the three configurations.

In the annular bright-field image, an abundance of surface V_O is shown embedded in a distinct area of high Zn content. The O/Zr ratio in the surface region (the outmost layers of three to four atoms) is slightly lower than that in the bulk (Supporting Information Figure S8), which is consistent with the XPS results showing that the enrichment of Zn dopants at the surface induces enrichment of oxygen vacancy. Overall, the above atomic-scale microstructure analysis indicates that the coordination environment of metal ions at the surface is derived as a function of Zn content in the solid solution, and the LD between neighboring Zn dopants serves as a critical factor governing the intrinsic properties of the surface coordination configurations.

Activation of CO_2 and H_2 on catalysts

We further investigated the activation of CO_2 and H_2 on the catalysts. The CO_2-temperature program desorption (TPD) results show that there are two desorption peaks for all catalysts: a low-temperature peak (below 340 °C), and a high-temperature peak (above 340 °C)

DOI: 10.31635/ccschem.024.202404243
Citation: *CCS Chem.* **2024**, 6, 2996–3007
Link to VoR: https://doi.org/10.31635/ccschem.024.202404243

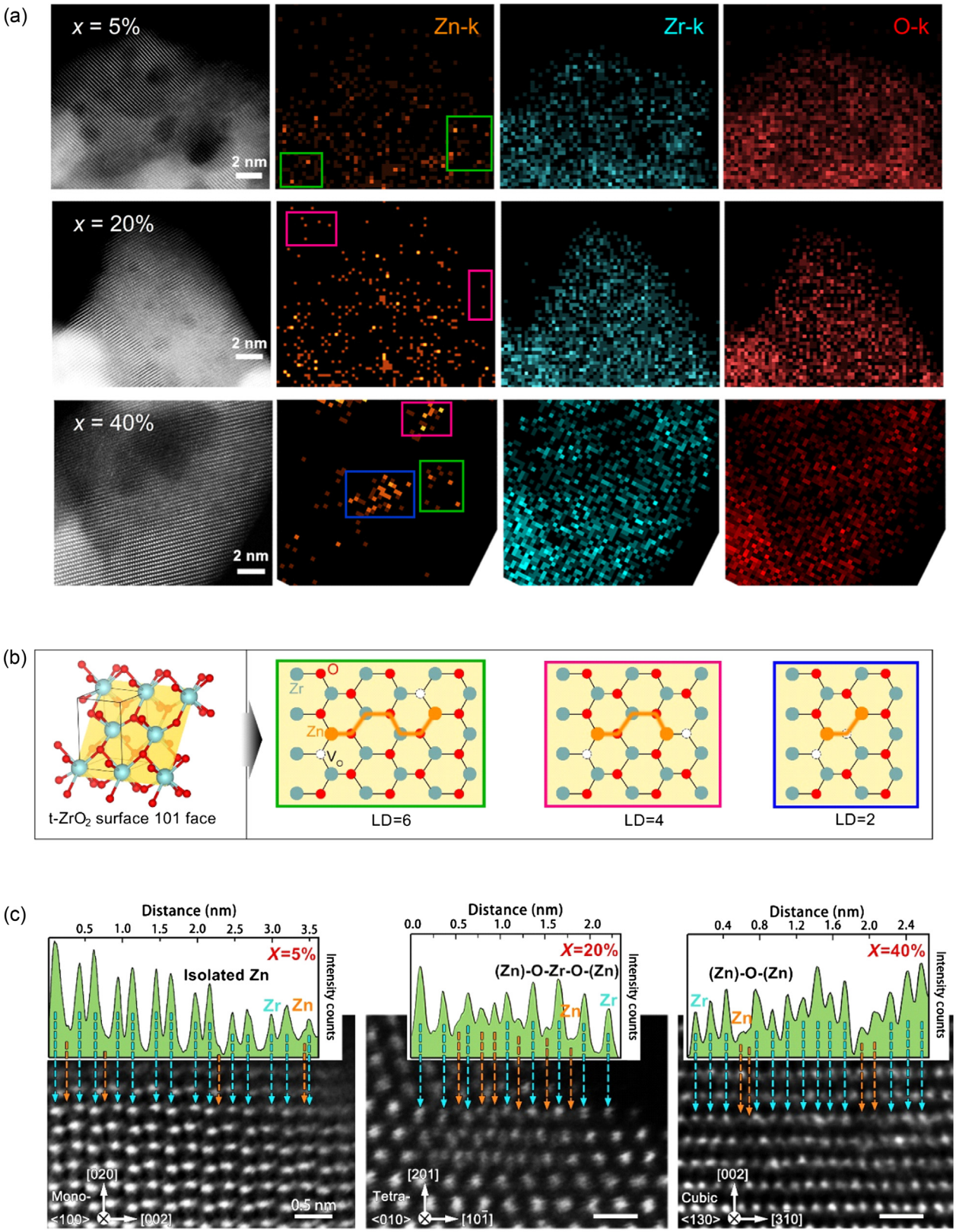

Figure 2 | *Characterization of coordination configurations near the surface. (a) EDS mappings of AC-STEM for 5% ZnO-ZrO_2, 20%ZnO-ZrO_2 and 40%ZnO-ZrO_2 samples. (b) Proposed configurations with different LD between Zn ions at t-ZrO_2 surface. Different colored borders correspond to areas in (a). Orange ball: Zn atom, Cyan ball: Zr atom; Red ball: O atom. (c) HAADF images of 5%ZnO-ZrO_2, 20%ZnO-ZrO_2 and 40%ZnO-ZrO_2 samples. The scale bars are all 0.5 nm.*

DOI: 10.31635/ccschem.024.202404243
Citation: *CCS Chem.* **2024**, 6, 2996–3007
Link to VoR: https://doi.org/10.31635/ccschem.024.202404243

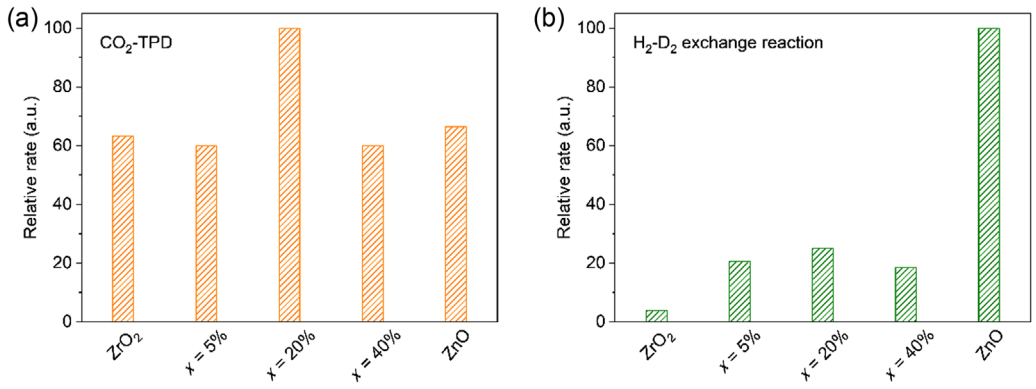

Figure 3 | *Activation of CO_2 and H_2 on ZnO-ZrO_2 solid-solution catalysts. (a) CO_2-TPD on pure ZrO_2, ZnO, and ZnO-ZrO_2 solid solution. (b) H_2–D_2 exchange reaction on pure ZrO_2, ZnO. and ZnO-ZrO_2 solid solution.*

(Supporting Information Figure S9). The low-temperature peak is more related to the CO_2 hydrogenation reaction since the reaction temperature is not higher than 320 °C. After the adsorption capacity is normalized by surface area (Supporting Information Table S3), we can see that ZrO_2 and ZnO adsorb similar amounts of CO_2 for the low-temperature peak (Figure 3a), while the 20%ZnO-ZrO_2 catalyst exhibits CO_2 much more strongly than the others. This may be related to the basicity of metal oxide and the amounts of V_O on the surface.[32–34] In addition, CO_2 is activated by the oxide catalysts in the form of carbonate or hydrocarbonate species (Supporting Information Figure S10). The H_2 activation can be estimated by the H_2–D_2 exchange reaction (Supporting Information Figure S11). Figure 3b shows that ZnO has a much stronger ability for H_2 activation than ZrO_2 per square meter, indicating the essential role of Zn sites in H_2 activation on the solid solution ZnO-ZrO_2 catalyst. The activity of 20%ZnO-ZrO_2 is greater than 5%ZnO-ZrO_2 and 40%ZnO-ZrO_2. The ability to activate hydrogen for each Zn atom has a distinct transition at 20% ZnO-ZrO_2. We can infer that the electronic property of Zn or Zr must be changed in ZnO-ZrO_2 solid solution. XPS (Supporting Information Figure S12) shows that the binding energies of Zn in 5–40%ZnO-ZrO_2 are lower than they are in ZnO, while the binding energies of Zr in 50–80%ZnO-ZrO_2 are lower than they are in ZrO_2. Therefore, it is suggested that the property of Zn in ZrO_2-based solid solution is changed, and the Zn site is responsible for activation of H_2.

DFT calculations

DFT calculations elucidate how the catalytic activity is tuned by the surface local atomic configuration of ZnO-ZrO_2 catalysts. Figure 4a shows the random distribution of Zn and Zr at the (101) surface in the tetragonal phase. With increasing Zn content, the LD between each pair of the nearest Zn atoms at the surface is reduced from predominantly 6 or higher to 4 and then to 2, and the atomic structures shown are adopted for the following calculations of coordination configurations representing isolated Zn, (Zn)-O-Zr-O-(Zn) and (Zn)-O-(Zn), respectively.

On the Zn-O site at the surface, the H_2 molecule heterolytically dissociates into a H^- (bonded to Zn) and a H^+ (bonded to a neighboring O), as demonstrated from the charge density difference plot in Figure 4b. This result holds regardless of the content of surface Zn, which suggests that the H^- attacks the carbon atom of adsorbed carbonate while the transfer of a proton to the oxygen atom of the carbonate species is simultaneously accompanied (Figure 4c). It is noted that the lowest unoccupied molecular orbital (LUMO) of CO_2 in the linear geometry is degenerate, which undergoes an orbital splitting upon molecular bending.[35] One of the orbitals drops in energy, providing the possibility for electron transfer during the first hydrogenation step of CO_2, in which the H^- contributes to the formation of a C–H covalent bond. This scenario is substantiated by the fact that the H^- on Zn can facilitate the first hydrogenation step. In the CO_2-to-methonal reaction (Figure 4c), two main stages are involved: (1) $CO_2 \rightarrow HCOOH \rightarrow H_2COOH^*$, in which the O–C–O moiety is highly bent (~127°), and (2) $H_2CO^* \rightarrow H_3COH^*$, where the O atom is attached to the surface. On the Zn-O site, H_2 dissociation is exothermic in free energy over a low energy barrier of 0.25 eV. In comparison, the energy consumption of H_2 dissociation on a Zr-O site is much higher (0.60 eV), and after dissociation, both H adatoms could readily recombined with an extremely low kinetic barrier (Supporting Information Figure S13). Therefore, Zn atoms are indispensable, not only for driving the phase transition of ZrO_2, but also for heterolytic cleavage of H_2 for the initiation reduction of CO_2.

We find that the formation of HCOO* intermediate generally exhibits a large energy release (Figure 4d and Supporting Information Figures S14–S16). This highly

DOI: 10.31635/ccschem.024.202404243
Citation: *CCS Chem.* **2024**, 6, 2996–3007
Link to VoR: https://doi.org/10.31635/ccschem.024.202404243

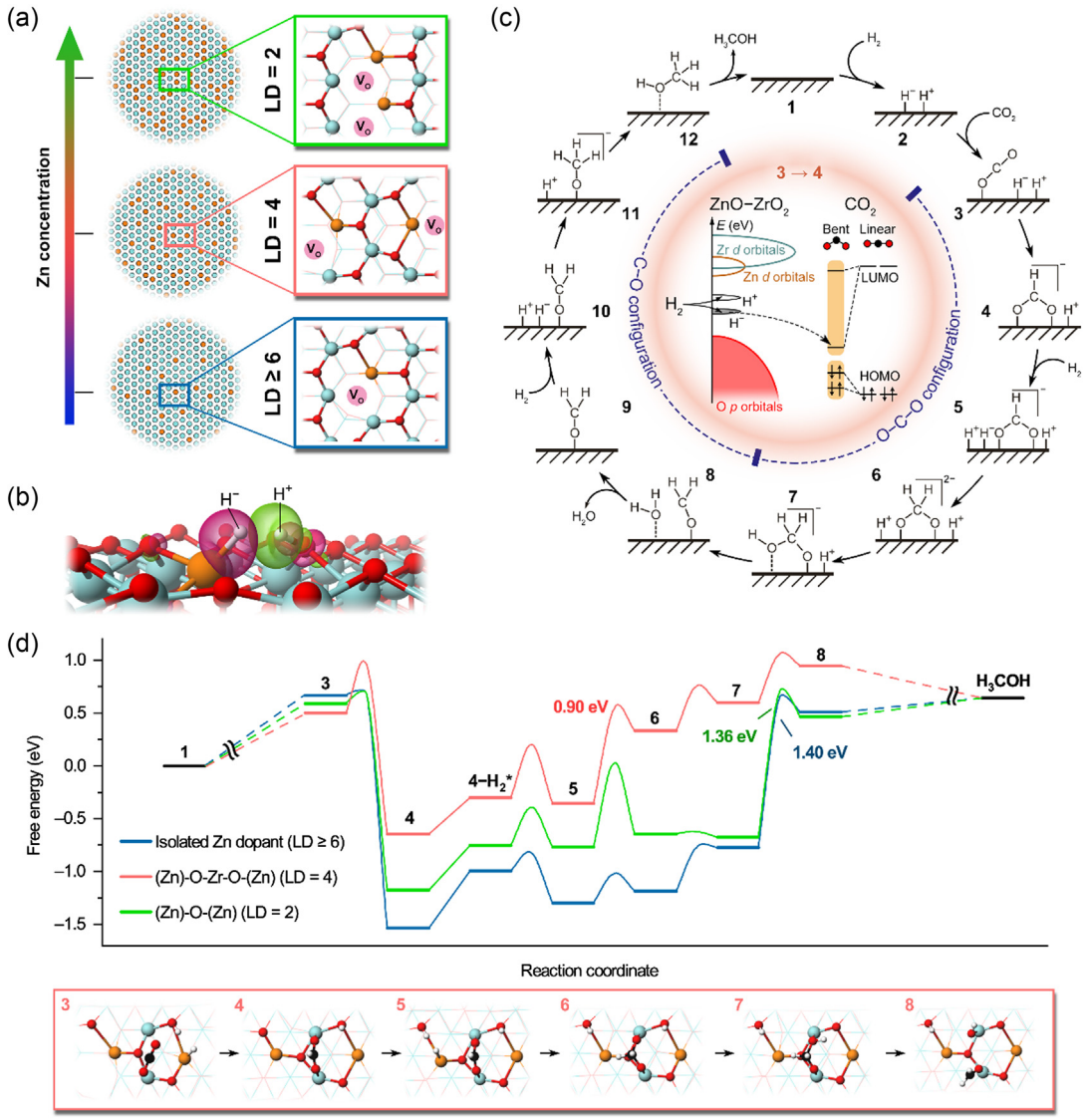

Figure 4 | *CO_2-to-methenal reaction mechanism on the catalytic sites with different coordination configurations at the surface. (a) Schematics of cation distributions on the (101) surfaces of the tetragonal ZnO-ZrO_2 catalysts with different Zn contents. The surfaces are featured by isolated Zn (LD ≥ 6), (Zn)-O-Zr-O-(Zn) (LD = 4), and (Zn)-O-(Zn) (LD = 2) coordination configurations. Only atoms in the surface layer are shown in spheres, while the structure beneath the surface is represented by wireframe. (b) Spatial distribution of charge density difference for the configuration after H_2 dissociation on Zn. Pink and green isosurfaces denote areas of charge accumulation and depletion (±0.05 e Å^{-3}), respectively, corresponding to the formation of H^- and H^+ ions. (c) Schematic reaction path and an illustration of electron transfer in the first hydrogenation step (in the middle circle). The highest occupied molecular orbital and the LUMO of CO_2 are indicated, both consisting of the $2p_x$ and $2p_y$ orbitals. (d) The free-energy diagrams of methanol production at 593 K on isolated Zn, (Zn)-O-Zr-O-(Zn), and (Zn)-O-(Zn). The lower panel shows the atomic structures of the corresponding reaction intermediates. Color code: Zr, cyan; Zn, orange; O, red; C, black; H, white.*

exothermic step gives rise to a large energy uptake in one of the subsequent steps since the overall reaction of CO_2 hydrogenation to methanol is endothermic. For the isolated Zn case (Supporting Information Figures S17–S19), the rate-determining step (RDS), that is, the **7** → **8** step, which happens to be the transition point between two reaction processes, is characterized by a free-energy barrier of 1.40 eV. For the (Zn)-O-(Zn) configuration (Supporting Information Figures S20–S22), the adsorption structures of all the intermediates bear a strong resemblance to those for isolated Zn, and therefore their energy profiles are quite similar. Yet, the barrier of RDS for (Zn)-O-(Zn) is slightly lower (1.36 eV), owing to the higher energy of the H_2COOH^* configuration, where only one Zr-O bond exists between the intermediate and the catalytic center, as compared to two bonds on isolated

DOI: 10.31635/ccschem.024.202404243
Citation: *CCS Chem.* **2024**, 6, 2996–3007
Link to VoR: https://doi.org/10.31635/ccschem.024.202404243

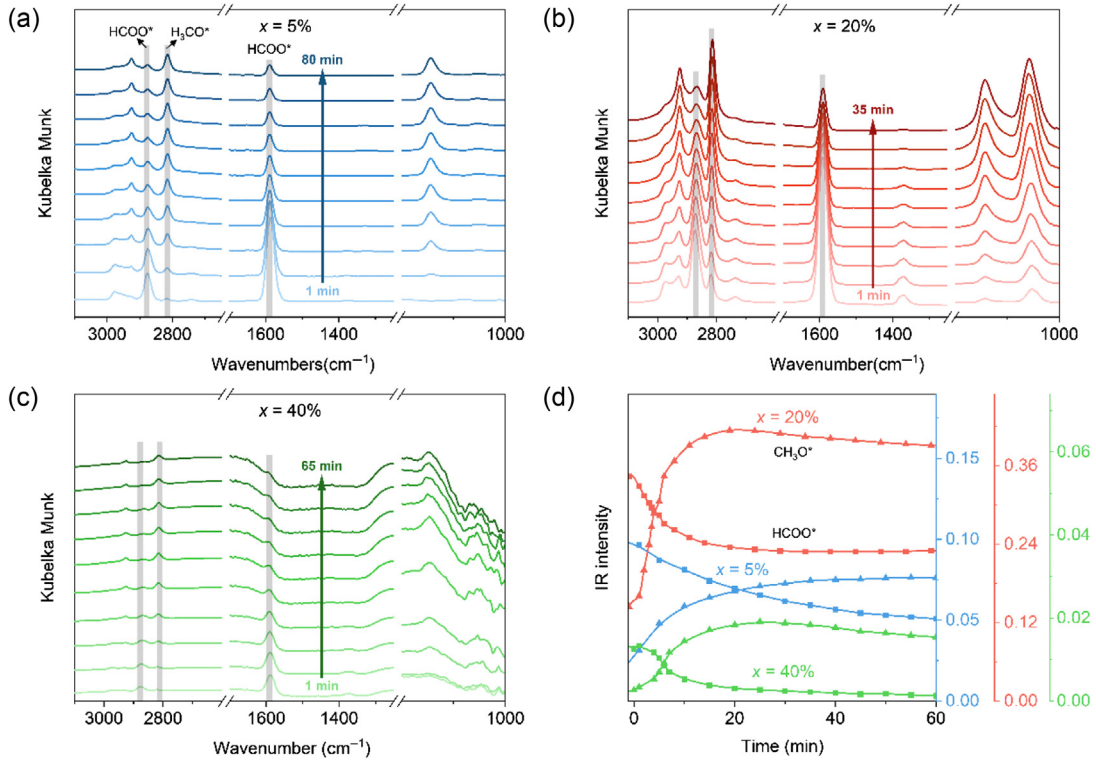

Figure 5 | *In-situ DRIFT spectra of surface species. (a) 5%ZnO-ZrO_2, (b) 20%ZnO-ZrO_2, and (c) 40%ZnO-ZrO_2. The gas is switched to H_2 for the catalysts with preadsorbed CO_2 + H_2. (d) The variation of surface species for the three ZnO-ZrO_2 catalysts.*

Zn (Supporting Information Figures S20 and S23). Interestingly, for the (Zn)-O-Zr-O-(Zn) configuration, the **7** → **8** step can proceed with a remarkably low barrier, while the **5** → **6** step becomes the RDS, with an energy barrier of 0.90 eV. The high activity can be ascribed to the reduced stability of reaction intermediates **4** to **7**, which leads to an overall flattening of the energy profile. The (Zn)-O-Zr-O-(Zn) active site has the merit of possessing two Zn_{Zr} catalytic centers that guarantee ample sites for the accommodation of dissociated H. These features participate in the bifunctional mechanism in which Zn dopants act as the H^- pumps and the confined domain of ZrO_2 between two Zn dopants serves as the effective site for CO_2 adsorption and subsequent CO_2 hydrogenation.

Surface species variation on catalysts

In-situ diffuse reflectance infrared Fourier transform spectroscopy (DRIFTS) results provide more evidence for the above mechanistic insights (Figure 5). The peaks at 2875 and 2819 cm^{-1} can be attributed to HCOO* (intermediate **4**) and H_3CO* (intermediate **11**) species, respectively (Supporting Information Figure S23 and Table S4).[36–38] The strong intensity of these peaks indicates the high stability of both HCOO* and H_3CO*, in agreement with the fact that they are located at the valleys of the reaction energy profiles (Figure 4d and Supporting Information Figures S13, S16, and S19). The concentrations of both species reach a steady state after reaction. We note that the 20%ZnO-ZrO_2 sample exhibits higher concentrations of these intermediates than 5% ZnO-ZrO_2 and 40%ZnO-ZrO_2, which is consistent with the superior catalytic activity of the former. The intensity of HCOO* decreases, and the intensity of H_3CO* increases when the reaction gas switches to H_2 (Figure 5a–c). This suggests the facile conversion of HCOO* to H_3CO* upon hydrogenation, thus justifying the format pathway of CO_2-to-methanol reaction as presented in the DFT calculations. Comparison of the increase rate of CH_3O* among three compositions (Figure 5d) highlight the optimal conversion rate and methanol selectivity at x = 20%, which is in line with the above experimental results.

Conclusion

Using a combination of neutron diffraction, atomic-resolution microscopy, in-situ spectroscopy, and theoretical modeling, we have identified the bifunctional surface active sites of ZnO-ZrO_2 solid solution catalysts and established the underlying relationship between the Zn-O-Zr site and catalytic performance. At the

DOI: 10.31635/ccschem.024.202404243
Citation: *CCS Chem.* **2024**, 6, 2996–3007
Link to VoR: https://doi.org/10.31635/ccschem.024.202404243

composition with optimal performance, that is, ~20% ZnO-ZrO_2, the coordination configuration of (Zn)-O-Zr-O-(Zn) prevails at the catalyst surface and functions as the active site for CO_2 hydrogenation to methanol. Zn dopants enable the dissociation of H_2 and facilitate the transfer of H^- ions to the reaction intermediates, while the confined domain of ZrO_2 between two Zn dopants yields a flattened energy landscape for the accommodation of the reaction intermediates. Their interplay steers the reaction towards methanol production, with a much lower activation barrier than isolated Zn sites and dinuclear Zn sites [in the configuration of (Zn)-O-(Zn)]. Our findings have far-reaching implications for how the synergetic effect of dual active sites in catalysts can be rationally designed to create effective bifunctional active sites for CO_2 hydrogenation to methanol.

Supporting Information

Supporting Information is available and includes Figures S1–S23 and Tables S1–S4.

Conflict of Interest

There is no conflict of interest to report.

Funding Information

This work was supported financially by grants from the Fundamental Research Center of Artificial Photosynthesis (grant no. 22088102), the Natural Science Foundation of China (grant no. 22172160), the Clean Energy Pilot Project of Chinese Academy of Sciences (CAS) (grant no. XDA0400303), and the Outstanding Member Youth Innovation Promotion Association CAS.

Acknowledgments

The authors thank Prof. R. Si for the help with the EXAFS measurements and data analysis.

References

1. Olah, G. A. Beyond Oil and Gas: The Methanol Economy. *Angew. Chem. Int. Ed.* **2005**, *44*, 2636–2639.
2. Shih, C.; Zhang, T.; Li, J.; Bai, C. Powering the Future with Liquid Sunshine. *Joule* **2018**, *2*, 1925–1949.
3. Wang, J.; Han, Z.; Chen, S.; Tang, C.; Sha, F.; Tang, S.; Yao, T.; Li, C. Liquid Sunshine Methanol. *Chem. Ind. Eng. Prog.* **2022**, *41*, 1309–1317.
4. Wang, J.; Li, G.; Li, Z.; Tang, C.; Feng, Z.; An, H.; Liu, H.; Liu, T.; Li, C. A Highly Selective and Stable ZnO-ZrO_2 Solid Solution Catalyst for CO_2 Hydrogenation to Methanol. *Sci. Adv.* **2017**, *3*, e1701290.
5. Wang, J.; Tang, C.; Li, G.; Han, Z.; Li, Z.; Liu, H.; Cheng, F.; Li, C. High-Performance M_aZrOx (M_a=Cd, Ga) Solid-Solution Catalysts for CO_2 Hydrogenation to Methanol. *ACS Catal.* **2019**, *9*, 10253–10259.
6. Han, Z.; Tang, C.; Sha, F.; Tang, S.; Wang, J.; Li, C. CO_2 Hydrogenation to Methanol on ZnO-ZrO_2 Solid Solution Catalysts with Ordered Mesoporous Structure. *J. Catal.* **2021**, *396*, 242–250.
7. Sha, F.; Tang, C.; Tang, S.; Wang, Q.; Han, Z.; Wang, J.; Li, C. The Promoting Role of Ga in $ZnZrO_x$ Solid Solution Catalyst for CO_2 Hydrogenation to Methanol. *J. Catal.* **2021**, *404*, 383–392.
8. Graciani, J.; Mudiyanselage, K.; Xu, F.; Baber, A. E.; Evans, J.; Senanayake, S. D.; Stacchiola, D. J.; Liu, P.; Hrbek, J.; Sanz, J. F.; Rodriguez, J. A. Highly Active Copper-Ceria and Copper-Ceria-Titania Catalysts for Methanol Synthesis from CO_2. *Science* **2014**, *345*, 546–550.
9. Kondrat, S. A.; Smith, P. J.; Wells, P. P.; Chater, P. A.; Carter, J. H.; Morgan, D. J.; Fiordaliso, E. M.; Wagner, J. B.; Davies, T. E.; Lu, L.; Bartley, J. K.; Taylor, S. H.; Spencer, M. S.; Kiely, C. J.; Kelly, G. J.; Park, C. W.; Rosseinsky, M. J.; Hutchings, G. J. Stable Amorphous Georgeite as a Precursor to a High-Activity Catalyst. *Nature* **2016**, *531*, 83–87.
10. Behrens, M.; Studt, F.; Kasatkin, I.; Kühl, S.; Hävecker, M.; Abild-Pedersen, F.; Zander, S.; Girgsdies, F.; Kurr, P.; Kniep, B.-L.; Tovar, M.; Fischer, R. W.; Nørskov, J. K.; Schlögl, R. The Active Site of Methanol Synthesis over Cu/ZnO/Al_2O_3 Industrial Catalysts. *Science* **2012**, *336*, 893–897.
11. Kuld, S.; Thorhauge, M.; Falsig, H.; Elkjær, C. F.; Helveg, S.; Chorkendorff, I.; Sehested, J. Quantifying the Promotion of Cu Catalysts by ZnO for Methanol Synthesis. *Science* **2016**, *352*, 969–974.
12. Kattel, S.; Ramirez, P. J.; Chen, J. G.; Rodriguez, J. A.; Liu, P. Active Sites for CO_2 Hydrogenation to Methanol on Cu/ZnO Catalysts. *Science* **2017**, *355*, 1296–1299.
13. Amann, P.; Klötzer, B.; Degerman, D.; Köpfle, N.; Götsch, T.; Lömker, P.; Rameshan, C.; Ploner, K.; Bikaljevic, D.; Wang, H.; Soldemo, M.; Shipilin, M.; Goodwin, C. M.; Gladh, J.; Stenlid, J. H.; Börner, M.; Schlueter, C.; Nilsson, A. The State of Zinc in Methanol Synthesis over a Zn/ZnO/Cu(211) Model Catalyst. *Science* **2022**, *376*, 603–608.
14. Sun, K.; Fan, Z.; Ye, J.; Yan, J.; Ge, Q.; Li, Y.; He, W.; Yang, W.; Liu, C. Hydrogenation of CO_2 to Methanol over In_2O_3 Catalyst. *J. CO_2 Util.* **2015**, *12*, 1–6.
15. Li, C.; Melaet, G.; Ralston, W. T.; An, K.; Brooks, C.; Ye, Y.; Liu, Y.; Zhu, J.; Guo, J.; Alayoglu, S.; Somorjai, G. A. High-Performance Hybrid Oxide Catalyst of Manganese and Cobalt for Low-Pressure Methanol Synthesis. *Nat. Commun.* **2015**, *6*, 6538.
16. Wang, L.; Guan, E.; Wang, Y.; Wang, L.; Gong, Z.; Cui, Y.; Meng, X.; Gates, B. C.; Xiao F. Silica Accelerates the Selective Hydrogenation of CO_2 to Methanol on Cobalt Catalysts. *Nat. Commun.* **2020**, *11*, 1033.
17. Hu, J.; Yu, L.; Deng, J.; Wang, Y.; Cheng, K.; Ma, C.; Zhang, Q.; Wen, W.; Yu, S.; Pan, Y.; Yang, J.; Ma, H.; Qi, F.; Wang, Y.; Zheng, Y.; Chen, M.; Huang, R.; Zhang, S.; Zhao, Z.; Mao, J.; Meng, X.; Ji, Q.; Hou, G.; Han, X.; Bao, X.; Wang, Y.; Deng, D. Sulfur Vacancy-Rich MoS_2 as a Catalyst for the

DOI: 10.31635/ccschem.024.202404243
Citation: *CCS Chem.* **2024**, 6, 2996–3007
Link to VoR: https://doi.org/10.31635/ccschem.024.202404243

Hydrogenation of CO_2 to Methanol. *Nat. Catal.* **2021**, *4*, 242–250.
18. Wang, J.; Meeprasert, J.; Han, Z.; Wang, H.; Feng, Z.; Tang, C.; Sha, F.; Tang, S.; Pidko, E. A.; Li, C. Highly Dispersed Cd Cluster Supported on TiO_2 as an Efficient Catalyst for CO_2 Hydrogenation to Methanol. *Chin. J. Catal.* **2022**, *43*, 761–770.
19. Meng, C.; Zhao, G.; Shi, X.; Chen, P.; Liu, Y.; Lu, Y. Oxygen-Deficient Metal Oxides Supported Nano-Intermetallic $InNi_3C_{0.5}$ Toward Efficient CO_2 Hydrogenation to Methanol. *Sci. Adv.* **2021**, *7*, eabi6012.
20. Zhang, J.; An, B.; Li, Z.; Cao, Y.; Dai, Y.; Wang, W.; Zeng, L.; Lin, W.; Wang, C. Neighboring Zn–Zr Sites in a Metal–Organic Framework for CO_2 Hydrogenation. *J. Am. Chem. Soc.* **2021**, *143*, 8829–8837.
21. Tada, S.; Ochiai, N.; Kinoshita, H.; Yoshida, M.; Shimada, N.; Joutsuka, T.; Nishijima, M.; Honma, T.; Yamauchi, N.; Kobayashi, Y.; Iyoki, K. Active Sites on $Zn_xZr_{1-x}O_{2-x}$ Solid Solution Catalysts for CO_2-to-Methanol Hydrogenation. *ACS Catal.* **2022**, *12*, 7748–7759.
22. Temvuttirojn, C.; Poo-arporn, Y.; Chanlek, N.; Cheng, C.; Chong, C.; Limtrakul, J.; Witoon, T. Role of Calcination Temperatures of ZrO_2 Support on Methanol Synthesis from CO_2 Hydrogenation at High Reaction Temperatures over ZnO_x/ZrO_2 Catalysts. *Ind. Eng. Chem. Res.* **2020**, *59*, 5525–5535.
23. Zhang, J.; An, B.; Cao, Y.; Li, Z.; Chen, J.; He, X.; Wang, C. ZnO Supported on a Zr-Based Metal–Organic Framework for Selective CO_2 Hydrogenation to Methanol. *ACS Appl. Energy Mater.* **2021**, *4*, 13567–13574.
24. Lin, L.; Wang, G.; Zhao, F. CO_2 Hydrogenation to Methanol on ZnO/ZrO_2 Catalysts: Effects of Zirconia Phase. *ChemistrySelect* **2021**, *6*, 2119–2125.
25. Salusso, D.; Borfecchia, E.; Bordiga, S. Combining X-Ray Diffraction and X-Ray Absorption Spectroscopy to Unveil Zn Local Environment in Zn-Doped ZrO_2 Catalysts. *J. Phys. Chem. C* **2021**, *125*, 22249–22261.
26. Kuhn, F.; Wattenhofer, R.; Zhang, Y.; Zollinger, A. Geometric Ad-Hoc Routing: Of Theory and Practice. In *Proceedings of the Twenty-Second Annual Symposium on Principles of Distributed Computing* ; New York: Association for Computing Machinery, **2003**; Vol. 3, pp 63–72.
27. Li, S.; Chen, Z.; Wang, Z.; Weng, M.; Li, J.; Zhang, M.; Lu, J.; Xu, K.; Pan, F. Graph-Based Discovery and Analysis of Atomic-Scale One-Dimensional Materials. *Natl. Sci. Rev.* **2022**, *9*, nwac028.
28. Kresse, G.; Furthmüller, J. Efficient Iterative Schemes for Ab Initio Total-Energy Calculations Using a Plane-Wave Basis Set. *Phys. Rev. B* **1996**, *54*, 11169–11186.
29. Perdew, J. P.; Burke, K.; Ernzerhof M. Generalized Gradient Approximation Made Simple. *Phys. Rev. Lett.* **1997**, *78*, 1396.
30. Henkelman, G.; Uberuaga, B. P.; Jonsson, H. A Climbing Image Nudged Elastic Band Method for Finding Saddle Points and Minimum Energy Paths. *J. Chem. Phys.* **2000**, *113*, 9901.
31. Igawa, N.; Ishii, Y. Crystal Structure of Metastable Tetragonal Zirconia Up to 1473 K. *J. Am. Ceram. Soc.* **2001**, *84*, 1169–1171.
32. Ghuman, K. K.; Hoch, L. B.; Wood, T. E.; Mims, C.; Singh, C. V.; Ozin, G. A. Surface Analogues of Molecular Frustrated Lewis Pairs in Heterogeneous CO_2 Hydrogenation Catalysis. *ACS Catal.* **2016**, *6*, 5764–5770.
33. Yu, K.; Lou, L.; Liu, S.; Zhou, W. Asymmetric Oxygen Vacancies: The Intrinsic Redox Active Sites in Metal Oxide Catalysts. *Adv. Sci.* **2020**, *7*, 1901970.
34. Cimino, A.; Stone, F. S. Oxide Solid Solutions as Catalysts. *Adv. Catal.* **2002**, *47*, 141–306.
35. Freund, H. J.; Roberts, M. W. Surface Chemistry of Carbon Dioxide. *Surf. Sci. Rep.* **1996**, *25*, 225–273.
36. Fisher, I. A.; Bell, A. T. In-Situ Infrared Study of Methanol Synthesis from H_2/CO_2 over Cu/SiO_2 and $Cu/ZrO_2/SiO_2$. *J. Catal.* **1997**, *172*, 222–237.
37. Kattel, S.; Yan, B.; Yang, Y.; Chen, J. G.; Liu, P. Optimizing Binding Energies of Key Intermediates for CO_2 Hydrogenation to Methanol over Oxide-Supported Copper. *J. Am. Chem. Soc.* **2016**, *138*, 12440–12450.
38. Feng, Z.; Tang, C.; Zhang, P.; Li, K.; Li, G.; Wang, J.; Feng, Z.; Li, C. Asymmetric Sites on the ZnZrOx Catalyst for Promoting Formate Formation and Transformation in CO_2 Hydrogenation. *J. Am. Chem. Soc.* **2023**, *145*, 12663–12672.

DOI: 10.31635/ccschem.024.202404243
Citation: *CCS Chem.* **2024**, 6, 2996–3007
Link to VoR: https://doi.org/10.31635/ccschem.024.202404243